Photoluminescence line shapes for color centers in silicon carbide from density functional theory calculations

Arsalan Hashemi,[1] Christopher Linderälv,[2] Arkady V. Krasheninnikov,[1,3] Tapio Ala-Nissila,[4,5] Paul Erhart,[2] and Hannu-Pekka Komsa[1,6]

[1]*Department of Applied Physics, Aalto University, P. O. Box 11100, 00076 Aalto, Finland*
[2]*Department of Physics, Chalmers University of Technology, Gothenburg 41296, Sweden*
[3]*Helmholtz-Zentrum Dresden-Rossendorf, Institute of Ion Beam Physics and Materials Research, 01328 Dresden, Germany*
[4]*QTF Centre of Excellence, Department of Applied Physics, Aalto University, FI-00076 Aalto, Finland*
[5]*Interdisciplinary Centre for Mathematical Modelling and Department of Mathematical Sciences, Loughborough University, Loughborough, Leicestershire LE11 3TU, UK*
[6]*Microelectronics Research Unit, University of Oulu, 90014 Oulu, Finland*

(Received 4 October 2020; revised 15 March 2021; accepted 15 March 2021; published 29 March 2021)

Silicon carbide with optically and magnetically active point defects offers unique opportunities for quantum technology applications. Since interaction with these defects commonly happens through optical excitation and deexcitation, a complete understanding of their light-matter interaction in general and optical signatures in particular is crucial. Here, we employ quantum mechanical density functional theory calculations to investigate the photoluminescence line shapes of selected, experimentally observed color centers (including single vacancies, double vacancies, and vacancy-impurity pairs) in 4H-SiC. The analysis of zero-phonon lines as well as Huang-Rhys and Debye-Waller factors is accompanied by a detailed study of the underlying lattice vibrations. We show that the defect line shapes are governed by strong coupling to bulk phonons at lower energies and localized vibrational modes at higher energies. Generally, good agreement with the available experimental data is obtained, and thus we expect our theoretical work to be beneficial for the identification of defect signatures in the photoluminescence spectra and thereby advance the research in quantum photonics and quantum information processing.

DOI: 10.1103/PhysRevB.103.125203

I. INTRODUCTION

During the past decade, improvements in the fabrication techniques of silicon carbide (SiC), a material with a wide electronic band gap of 3.2 eV [1], have made it possible to produce high-quality samples [2,3] with control over types and concentrations of color centers in this system, making SiC attractive for applications in nanophotonics, electronics, and spintronics [4–6]. These centers can potentially be used as single-photon sources and spin-photon interfaces [7–13], and thus they could play a central role in future quantum technologies [14–17]. Nowadays, it is also possible to prepare SiC with largely isolated color centers, which allows investigations of the properties of specific types of color centers [18,19].

SiC exists in several polytypes, with 3C, 4H, and 6H being the most common ones. The majority of the research on color centers for single-photon emitters and spin qubits reported in the literature has been carried out on 4H-SiC, as it is easy to synthesize in high quality and with a low density of stacking faults. 4H-SiC, which has a high Debye temperature of 1200 K [20] and strong second-order optical nonlinearity [21], consists of four SiC sheets stacked in ABCB order along the c-axis. It contains two nonequivalent hexagonal (h) and quasicubic (k) sites for each atom. In addition, different charge states can be favorable for some color centers [22,23]. As a result, 4H-SiC can host several defects with distinct photoluminescence (PL) peaks within the band gap. The most important ones are as follows: (i) The negatively charged silicon vacancy (V_{Si}^{-1}) in h or k sites with a zero-phonon line (ZPL) in the range of 1.352–1.445 eV [24–27]. It offers two excitation possibilities at each vacancy site. (ii) The neutral carbon-silicon divacancy (V_CV_{Si}) can occur in four distinct configurations (hh, hk, kh, and kk) and exhibits ZPL in the range of 1.095–1.15 eV [19,28–31]. Both V_{Si} and V_CV_{Si} are paramagnetic color centers and exhibit long spin coherence times [25,32]. (iii) The carbon antisite-vacancy pair (V_CC_{Si}) has been characterized in -1, 0, and $+1$ charge states [33–37]. (iv) The extrinsic negatively charged silicon vacancy-nitrogen pair ($V_{Si}N_C^{-1}$) is equivalent to the famous nitrogen-vacancy (NV) center in diamond [38,39] and emits light in the 1 eV range [40–43].

The experimentally measured PL spectra are defect-specific and originate from the combination of electronic transitions with phonons. While purely electronic transitions give rise to the so-called ZPLs, transitions that involve phonon creation or annihilation lead to the so-called phonon sideband (PSB), which is located at lower (higher) energies than the ZPL in photon emission (absorption) spectra. From the ZPL and PSB, one can extract the Huang-Rhys factor (HRF) and the Debye-Waller factor (DWF) [44], which are important

parameters to assess the suitability of defects for quantum applications. The DWF describes the relative ratio of light emitted in the ZPL relative to the total emitted light, and the HRF describes the average number of phonons involved in the emission. Thus, a larger DWF and a smaller HRF are obtained when the electron-phonon interaction is weaker, and they indicate a lower information leakage to the environment, which is important for the usage of color centers in quantum information science and nanosensing [45–47].

Although all these defects have been the subject of several publications, the experimental results are usually focused on an individual color center. The only well-reported signatures of defects are the spectrally narrow emission spectra at a certain wavelength at low temperatures [19,24–31,33–37,40–43]. Electronic structure calculations can be extremely useful to obtain detailed insight and understanding of defects, at a level inaccessible to experiment. Accordingly, they have been routinely used to analyze, e.g., charge transition levels, spin states, and ZPLs [22,23,28,48–50]. It was, however, only very recently [24,25] that the PSBs of V_{Si} were calculated and compared to experimental data. While DWFs were reported, the contributions from different vibrational modes to them remain poorly understood.

Here, to ameliorate this situation, we provide a comprehensive and systematic analysis of the vibrational signatures of all of the aforementioned defects. Using density functional theory (DFT) in combination with the generating function approach, we obtain the PSBs, ZPLs, DWFs, and HRFs and determine spin states and charge localization for each defect. These results are compared to experimental results, where available. We then analyze the vibrational modes via the electron-phonon coupling spectral function, and we separate localized vibrational modes from bulk phonons. Finally, we discuss our results in the context of technological applications.

II. METHODOLOGY

A. Generating function approach

PL line shapes, and the PSB in particular, are modeled via the generating function approach as described in Refs. [51–53]. To model the PSB, the electron-phonon interaction has to be accounted for. The interaction can be formalized using the partial HRF defined as

$$S_\lambda = \omega_\lambda Q_\lambda^2 / 2\hbar, \tag{1}$$

where $\hbar$ is the reduced Planck constant, and the configurational coordinate Q_λ for an optical process is defined as

$$Q_\lambda = \sum_\alpha \sqrt{m_\alpha} \langle (\mathbf{R}_{e,\alpha} - \mathbf{R}_{g,\alpha}) | \mathbf{u}_{\alpha,\lambda} \rangle. \tag{2}$$

Here, $\mathbf{R}_g$ and $\mathbf{R}_e$ are ground- and excited-state atomic coordinates, while $\mathbf{u}_{\alpha,\lambda}$ indicates the normalized displacement vector corresponding to mode λ with frequency ω_λ, and m_α is the mass of atom α. The total HRF and Q^2 are defined as $S = \sum S_\lambda$ and $Q^2 = \sum Q_\lambda^2$, respectively. They provide measures for the average number of phonons involved in the emission and the difference between the initial- and final-state geometries. From the HRF, the DWF can be defined as DWF $= \exp(-S)$ [53]. The spectral function that underlies the computation of the PSB is

$$S(\omega) = \sum_\lambda S_\lambda \delta(\omega - \omega_\lambda), \tag{3}$$

where the δ-function is replaced by a Gaussian with a broadening of 3 meV . Once the electron-phonon spectral function is computed, the spectral distribution function can be determined as

$$A(\omega) = \int dt \exp[S(t) - S(0)] \exp(i\omega t - \gamma |t|), \tag{4}$$

where $S(t)$ is the Fourier transform of $S(\omega)$, and $\gamma = 10^{-7}$ rad/s is set to reproduce the broadening of ZPLs. The emission intensity is proportional to $\omega^3 A(\omega)$.

B. Computational details

Electronic structure calculations were performed within the framework of DFT using the projector augmented wave method [54,55] as implemented in the Vienna ab-initio simulation package [56,57]. For structural relaxations and phonon calculations, the PBEsol exchange correlation functional was used [58]. To correct for the well-known band-gap error intrinsic to semilocal exchange-correlation functionals such as PBEsol, additional calculations were carried out using the HSE06 hybrid exchange correlation functional [59]. To obtain accurate transition energies and ZPLs, we (i) used PBEsol-optimized structures, (ii) scaled the lattice parameters to be consistent with the values from HSE06, and (iii) performed total energy calculations using HSE06 without further relaxation. Eventually, the ZPL value was calculated from the energy difference between the supercell in the ground and excited state. The plane-wave energy cutoff was set to 400 eV . Ionic optimization was performed until forces were smaller than 10 meV/Å, and the break condition for the electronic self-consistent loop was set to 10^{-6} eV. The first Brillouin zone of the primitive unit cell was sampled using a $10 \times 10 \times 4$ $\boldsymbol{k}$-point grid.

To model defects, $5 \times 5 \times 2$ supercells containing up to 400 atoms were used. The Brillouin zone was sampled using a zone centered $2 \times 2 \times 2$ grid and the Γ-point in PBEsol and HSE06 calculations, respectively. These supercells correspond to a defect concentration of about 2.5×10^{20} cm^{-3}. Spin-polarized calculations were performed for all charge states. To model optical transitions, we constrained the partial occupancies of the Kohn-Sham levels, promoting one electron from the highest occupied state to the next or second-next higher-energy state in the same spin channel. If the electron was promoted to a doubly degenerate state, we fixed the occupancy weight for each state to one-half to achieve faster convergence of the calculation [53].

The defects considered in this work are illustrated in Fig. 1. For Si vacancies, we include the singly negative charge state (V_{Si}^{-1}) positioned at both h and k sites, and the doubly negative charge state (V_{Si}^{-2}) at the k site [23,49]. Regarding divacancies ($V_C V_{Si}$), we study configurations comprising a Si vacancy on an h site in combination with C vacancies on either h or k sites. Finally, we include two variants of the NV center in diamond, namely the positively charged $V_C C_{Si}$ and the negatively charged $N_C V_{Si}$ complexes. In total, there are thus

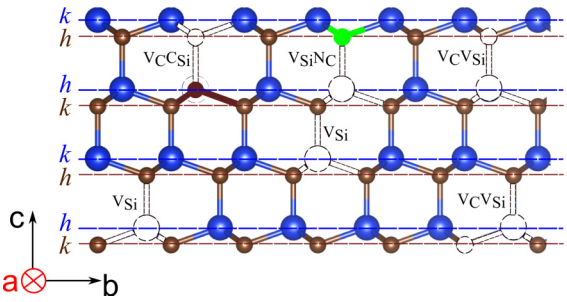

FIG. 1. Schematic representation of defect configurations in 4H-SiC. Blue, brown, and green spheres denote silicon, carbon, and nitrogen atoms, respectively. Vacancy sites are shown as hollow spheres. The planes labeled *h* and *k* indicate the symmetry of lattice sites.

seven centers and nine optical transitions possible (Fig. 2). All transitions are charge-neutral, i.e., they occur between two localized defect states of the same center. Here, in labeling the transitions we follow conventions adopted in earlier work in this field [22,29,35,36,41,61,62] except for the doubly negative silicon vacancy, V_{Si}^{-2}, at the *k* site, which we named W2.

Phonon calculations for large defect systems are computationally demanding. To accelerate these calculations, we used regression as implemented in the HIPHIVE package [63]. For each transition, training data were prepared by calculating the forces for the ground-state structure using up to 125 configurations with random displacements, which were drawn from a normal distribution with a standard deviation of 0.01 Å . The interatomic force constants (IFCs) were then reconstructed using a cluster basis set with second-order cutoffs of 4.2–5.0 Å and optimized by least-squares regression. For all cases, the root-mean-square error over a holdout set that comprised 5% of the total available data was 17 meV/Å or lower. Finally, the IFCs were used to compute phonon frequencies and eigenvectors with the PHONOPY package [64].

We benchmarked our approach by fully relaxing the atomic structure for the $N_C V_{Si}$ defect center using the HSE06 functional. The ZPL value changed from 1.28 (PBEsol + HSE06) to 1.32 eV (fully HSE06), and Q^2 changed from 0.70 (PBEsol + HSE06) to 0.69 (HSE06), indicating that the atomic structure and the vibrational properties of the defects are well captured by the PBEsol functional.

III. RESULTS

A. Electronic structures and excitations

The 4H-SiC structure has hexagonal symmetry with the lattice constants *a* and *c*. Our results obtained using the PBEsol functional for the lattice constants are $a = 3.08$ Å and $c = 10.08$ Å. The electronic band gap from HSE06 calculations is found to be $E_g = 3.25$ eV. These values are in good agreement with experimental data of $a = 3.09$ Å, $c = 10.48$ Å, and $E_g = 3.2$ eV [65].

The defects considered here exhibit at least one occupied and one unoccupied defect state in the band gap, comprising a two-level optical system that involves states localized

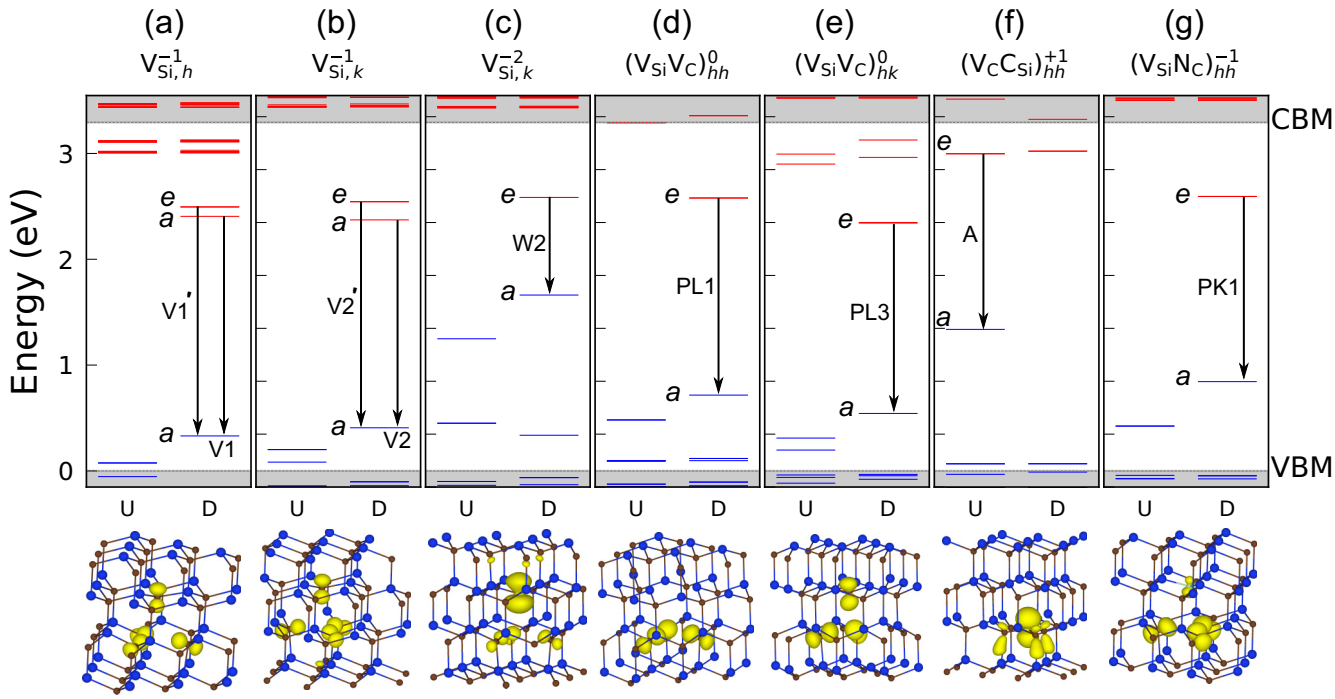

FIG. 2. Top: arrows show the optical excitation between the highest occupied (blue lines) and unoccupied KS levels (red lines). Doubly degenerate and nondegenerate states are denoted by *e* and *a*, respectively. After excitation, the electron decays to the ground electronic state by photon and phonon emission. The majority (spin-up) and minority (spin-down) channels are denoted by *U* and *D*, respectively. Bottom: the figure is created using the software VESTA [60]. Yellow isosurfaces illustrate partial charge densities of the highest occupied state in the transition channel for the ground-state configurations with the isosurface level set to 0.003 $e/Å^3$. Si, C, and N atoms are denoted by blue, brown, and green balls.

TABLE I. Key properties from calculation and experiment for the defect transitions considered here.

		ZPL (eV)		Q^2 (Å^2 amu)	HRF	DWF (%)	
		HSE06	Expt.	PBEsol	PBEsol	PBEsol	Expt.
V_{Si}^{-1}	V1	1.57	1.44 [24]	0.62	2.78	6.17	6–8 [24]
	V1′	1.60	1.44 [27]	0.66	2.77	6.23	
	V2	1.24	1.35 [24]	0.64	2.82	5.94	9.0 [25]
	V2′	1.28		0.47	1.94	14.34	
V_{Si}^{-2}	W2	0.72		0.30	1.47	22.97	
$V_C V_{Si}$	PL1	1.14	1.10 [29]	0.71	2.75	6.39	5.3 [32]
	PL3	1.25	1.12 [66]	0.99	3.08	4.57	5.0 [67]
$V_C C_{Si}$	A	1.69	1.88 [36]	0.73	3.77	2.29	
$N_C V_{Si}$	PK1	1.28	1.00 [41]	0.70	2.64	7.09	

in proximity to the defect. In Fig. 2 the electronic transitions are shown. Transitions are labeled in accordance with previous experimental studies except for V_{Si}^{-2}, for which no established label exists. All transitions were obtained by promoting an electron in the spin minority channels, except for configuration A, for which the optical transition occurs in the majority spin channel. The ground-state electronic configurations exhibit spin states $S = 3/2$, 1, 1, 1/2, and 1 for V_{Si}^{-1}, V_{Si}^{-2}, $V_C V_{Si}^{0}$, $V_C C_{Si}^{+1}$, and $V_{Si} N_C^{-1}$ centers, respectively. These values were experimentally and theoretically confirmed [22,35,40,61,62].

In the electronic ground state of V_{Si}^{-1} [Figs. 2(a) and 2(b)], four C dangling bonds point to the vacant site with their localized orbitals. V_{Si}^{-1} on an h site is associated with transitions V1 and V1′, which correspond to HOMO ← LUMO and HOMO ← LUMO + 1 transitions, respectively (HOMO denotes highest occupied molecular orbital, LUMO denotes lowest unoccupied molecular orbital). Analogously, V_{Si}^{-1} on a k site supports transitions V2 and V2′. The two transitions are separated by 116 and 172 meV, respectively, at h and k sites. The LUMO + 1 states are doubly degenerate. Here the excited state is constructed by equally occupying each degenerate orbital.

Upon addition of one extra electron to V_{Si}^{-1} to obtain V_{Si}^{-2}, the electrons are still localized next to the vacant site [Fig. 2(c)]. The charge distribution is mostly localized on the C atom placed at the same crystallographic site as vacant Si. In contrast to V_{Si}^{-1}, V_{Si}^{-2} can only host a single optical transition, labeled W2 for the k site. Previous formation energy calculations showed that the doubly negative Si vacancy is stable in charge state −2 [22], but the predicted PL line has not yet been experimentally observed. The W2 transition exhibits a ZPL energy of 0.72 eV, which is in the telecom wavelength (<1 eV).

The neutral divacancies [Figs. 2(d) and 2(e)] can exhibit different symmetries depending on the local symmetry of the vacancy C and Si atoms. To restrict ourselves, we consider the HOMO ← LUMO transitions on the divacancy in hh and hk.

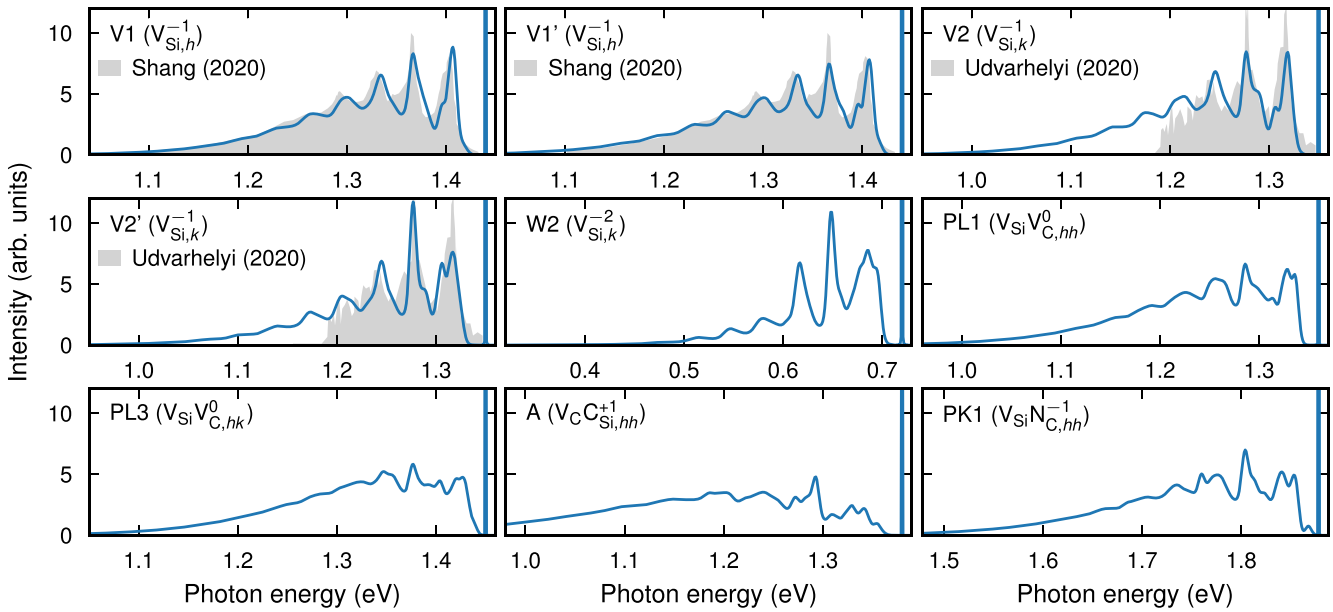

FIG. 3. Emission line shapes for the defect transitions considered in this study. The V1, V1′ and V2, V2′ (V_{Si}^{-1}) transitions are shifted to the respective experimental ZPLs in order to facilitate the comparison between calculation and experiment. Experimental data from Refs. [24] (Shang, 2020) and [25] (Udarvhelyi, 2020) measured at $T = 15$ and <30 K, respectively, are shown by the shaded areas. The intensity of the experimental line shapes from Ref. [25] has been scaled to match the peaks of the computed line shapes.

Based on the KS spectra, additional transitions are possible in both *hh* and *hk* symmetry. The HOMO ← LUMO transition on *hh* is labeled PL1 and the HOMO ← LUMO transition on *hk* is labeled PL3. The electronic charge is equally distributed among the C atoms nearest to the silicon vacancy. It is noteworthy that the three nearest Si and C neighbors to the C and Si vacancy, respectively, relax inward toward the respective vacant site by 0.02 Å .

The singly charged carbon vacancy-carbon antisite defect $V_C C_{Si}^{+1}$ supports one transition labeled A, which occurs between two localized levels in the majority spin channel [Fig. 2(f)]. Charge is mostly localized on the antisite carbon and to a lesser degree on its three nearest C neighbors. With 1.55 Å the C–C bond length is about 0.34 Å shorter than Si–C bonds in the ideal lattice.

Finally, the negatively charged silicon vacancy adjacent to a nitrogen atom that substitutes carbon, $V_{Si}N_C^{-1}$, which contains one additional electron compared to V_{Si}^{-1}, allows for a single optical transition based on the KS spectrum [Fig. 2], which is labeled PK1. Only a very small part of the density of the unpaired electrons is found at the N atom. The defect resembles the axial $V_C V_{Si}$ divacancy with the Si–N bond length being about 0.11 Å shorter than Si–C bonds in the ideal lattice.

Our calculated ZPL energies differ by less than 0.2 eV from the experimentally measured ones with the exception of the PK1 transition on $V_{Si}N_C^{-1}$ (Table I), a level of accuracy that matches earlier calculations [28]. Generally, the good agreement with experiment of the calculated ZPL energies, as well as some of the other defect properties to be considered in the following, validates the defect assignments given in the literature.

B. Luminescence line shapes

The calculated emission line shapes are shown in Fig. 3, where the ZPLs have been shifted to the respective experimental value to simplify the comparison where applicable. The emission spectra consist of a sharp ZPL followed by a *structured* PSB at lower energy. It is evident from the results for the individual defects that the PSBs share some features: (i) the ZPLs are separated from the PSBs by an energy gap of about 30 meV, (ii) the broadening of the PSBs ranges from 200 to 500 meV, corresponding to the respective HRFs (Table I), and (iii) smaller HRFs (the number of created phonons) are associated with more structured PSBs.

The strength of the electron-phonon coupling can be partly assessed by the Q^2 value (Table I), which measures the magnitude of the geometric difference between the initial and the final state. It varies from 0.4 to 1.0 Å^2 amu for the W2 (V_{Si}^{-2}) and PL3 ($V_C V_{Si}$) transitions showing the smallest and largest displacements, respectively. The DWF varies from 2% to 23%, with larger values implying a larger fraction of emission intensity in the ZPL. By this measure the V_{Si}^{-2} center, which has not been experimentally observed, should be the best single-photon emitter (SPE) candidate. The V2′ (V_{Si}^{-1}) transition results in a smaller lattice distortion at a value of 0.47 Å^2 amu compared with 0.61 − 0.67 Å^2 amu (Table I) for the other transitions on V_{Si}^{-1}. The PL1 ($V_C V_{Si}$), A ($V_C C_{Si}$), and PK ($N_C V_{Si}$) transitions exhibit the same Q^2 but differ in HRFs (PK1 ≈ PL1 < A). As a result, one observes rather similar line shapes, especially between PL1 and PK1, except for a hump at about 10 meV below the ZPL in the PK1 transition, which is due to a localized phonon. Although the inclusion of an adjacent V_C to the V_{Si} in the transitions PL1 and PL3 modifies the position of the ZPL, it does not induce a dramatic change in the emission line shape. The optical emission line shape of the transition A ($V_C C_{Si}$) with a tail of about 500 meV shows the widest PSB. We assign it to the contributions of high-energy phonons and stronger coupling between electrons and phonons during emission.

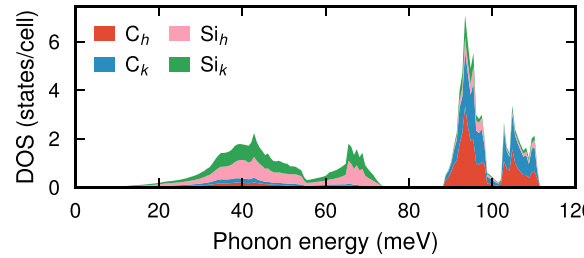

FIG. 4. Partial phonon densities of states for the ideal structure of 4H-SiC.

Our calculations for the V1/V1′ and V2/V2′ transitions involving V_{Si} defects are in excellent agreement with experimental data [24,25]. They yield similar line shapes, and the PSB width is about 300 meV . The comparison with experimental data can also be made by using the DWF (e^{-HRF}) values in Table I to benchmark our calculations. Overall, the calculations are in excellent agreement with experiments. The line shape of the A transition has been measured [36] at 120 K and was hypothesized to originate from the $V_C C_{Si}$ defect. The computed line shape does not agree favorably with that measurement, which poses the question whether the measured transition is actually taking place on $V_C C_{Si}$. Also the experimentally reported DWF for the A transition (1%) [36] deviates from our calculation (2.29%), which we attribute to the finite-temperature effect present in the experiments.

C. Vibrational modes analysis

Our phonon calculations for the pristine system using a primitive unit cell (PUC) give the high-energy Raman-active mode at 96.63 meV, which is in excellent agreement with the experimental value of 96.59 meV [69]. The phonon density of states (DOS) can be divided into two parts (Fig. 4). In the energy range up to 75 meV, the Si modes are dominant due to the larger mass of the Si atoms, while the double-peaked C-based modes are active at higher energies and centered at around 100 meV . The phonon band gap is about 14.2 meV starting from 76.4 meV . Note that we see a slight difference between the partial DOSs of atoms placed at *h* and *k* sites due to the different arrangement of second nearest neighbors.

To gain insight into the contribution of different vibrational modes to the PSBs, we now consider the electron-phonon coupling spectral functions [Eq. 3]. To evaluate the localization of the modes in more detail, we analyzed the inverse participation ratio (IPR) for the mode λ as [53,70]

$$\mathrm{IPR}_\lambda = \frac{1}{\sum_a |\mathbf{u}_{a,\lambda}|^2}. \tag{5}$$

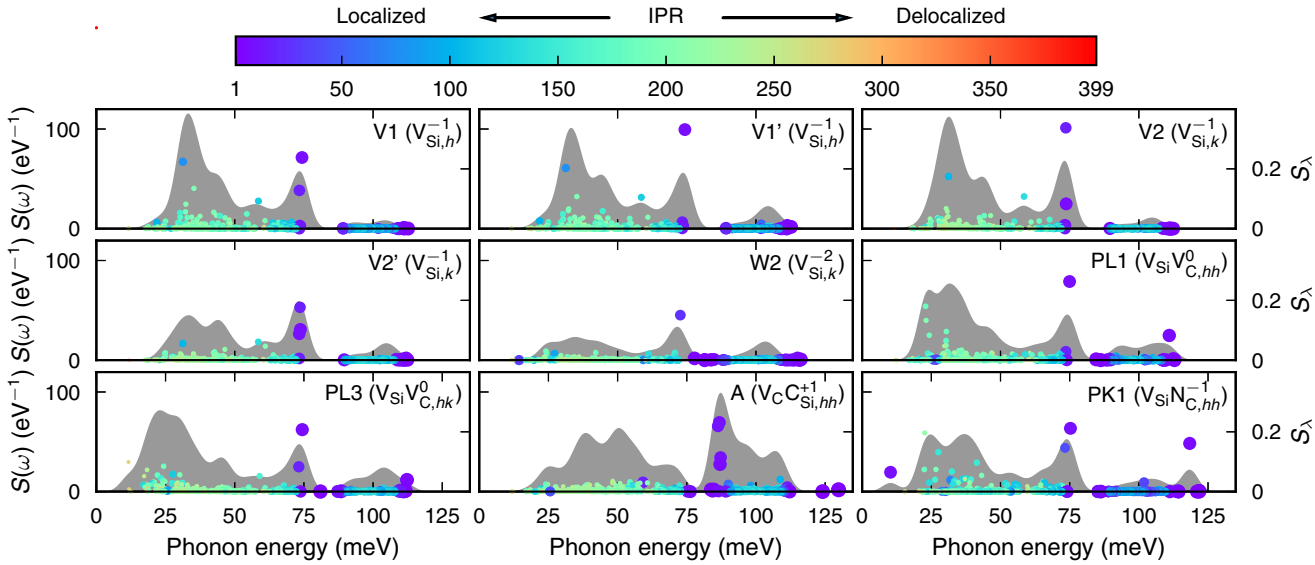

FIG. 5. Spectral functions $S(\omega)$ (gray, shaded areas) and partial HRFs (dots) for all considered defects. The IPRs associated with each mode are indicated both by color and by the size of the markers of the partial HRFs.

$\mathrm{IPR}_\lambda = 1$ if only one atom vibrates, while $\mathrm{IPR}_\lambda = N$ if all N atoms in the supercell vibrate with the same amplitude. Moreover, the localized vibrational modes that give rise to strong HRFs are collected and schematically illustrated.

The electron-phonon spectral functions are shown in Fig. 5, accompanied by the plots of partial HRFs and inverse participation ratio (IPR). The spectral function $S(\omega)$ for the transitions on V^{-1}_{Si} (V1, V1′, and V2) show only minor differences, while the V2′ transition can be clearly distinguished from the other three transitions. This is reflected in the HRF, which is about 2.8 for V1, V1′, and V2 while it is 1.9 for V2′.

Overall, the vibrational contribution to the transitions can be divided into the following: (i) Acoustic and optical bulk modes with energy less than 45 meV, e.g., the V1, V1′, and V2 transitions, and to a lesser extent the V2′ transition, which exhibits a pronounced peak at 35 meV . This peak is composed of several modes with IPR > 100 (the maximal value of the IPR for this cell is 399). (ii) Defect modes that are mostly located around the lower edge of the phonon band gap. In the V2 transition, the 73 meV peak can be attributed to two modes with relatively low IPR values of 8 and 18. In V2′, there are three modes (IPR between 9 and 18) that have HRFs between 0.09 and 0.18, making the total coupling in the region around 73 meV similar in strength to the other transitions. We note that there are many well-localized modes (IPR$\sim$4–6) at the high-frequency edge $\sim$110 meV in all transitions on V^{-1}_{Si}. These modes do not, however, couple strongly to the transition displacement since the phonon displacement vectors are nearly perpendicular to the transition displacement. The W2 transition (V^{-2}_{Si}) resembles the V2′ spectral function with a weaker coupling to the vibrational degrees of freedom as indicated by the small total HRF of 1.47.

The coupling to the vibrational modes is similar between the transitions on divacancies (PL1 and PL3), as is evident from the spectral functions and the similar HRFs of 2.75 and 3.08, respectively. The general features of the spectral functions are similar to the transitions on V^{-1}_{Si}, except for the broader peaks at 20–50 meV . The strongest coupling is at 75 meV in both PL1 and PL3. The mode is a low IPR mode with values of 8 and 7 in PL1 and PL3, respectively. In addition, the spectral weight in the high-frequency range, around 100 meV, is slightly larger compared to the case of V^{-1}_{Si}. The peaks centered at 23, 35, and 48 meV originate predominantly from several delocalized (bulk) modes with IPR > 100.

In the case of the A transition, the coupling to the localized vibrational modes is much larger than with other considered transitions. The strongest coupling is to a set of four quasidegenerate modes at the upper edge of the phonon band gap (86–87 meV) with partial HRFs between 0.09 and 0.23. For PK1 ($N_C V_{Si}$), the coupling to the vibrational modes consists of three distinct bands at around 20–50, 75, and 120 meV . The localized vibrational mode around 10.3 meV is absent in other intrinsic centers. Its IPR value is 9. The peak centered at 75 meV results mainly from the coupling of two modes at 73 and 75 meV with HRFs of 41 and 8, respectively.

The selected vibrational modes and atomic displacements due to electron excitation are shown in Fig. 6. The dominant geometrical difference between the ground and excited states for all transitions on V^{-1}_{Si} is the radial motion (relative to the vacancy) of nearest-neighbor carbon atoms, which are displaced by 0.08 Å in the case of V1 and 0.05 Å in the case of V1′. For V2, the displacements of atoms after relaxation for these defects are inward upon emission. These modes are quasidegenerate and consist predominantly of the motion of the nearest (relative to the vacancy) carbon atoms. The intensity of the 73 meV peak in the spectral function is, however, not much weaker in the case of V2′ compared with the other transitions (V1, V1′, V2), although the displacement of the nearest-neighbor carbon atom is smaller. For PL1, the phonon displacement for the 75 meV localized mode is shown in Fig. 6. During the transition, the closest C atoms to the silicon vacancy undergo the largest displacements toward the vacancy, while the Si atoms next to the C vacancy move

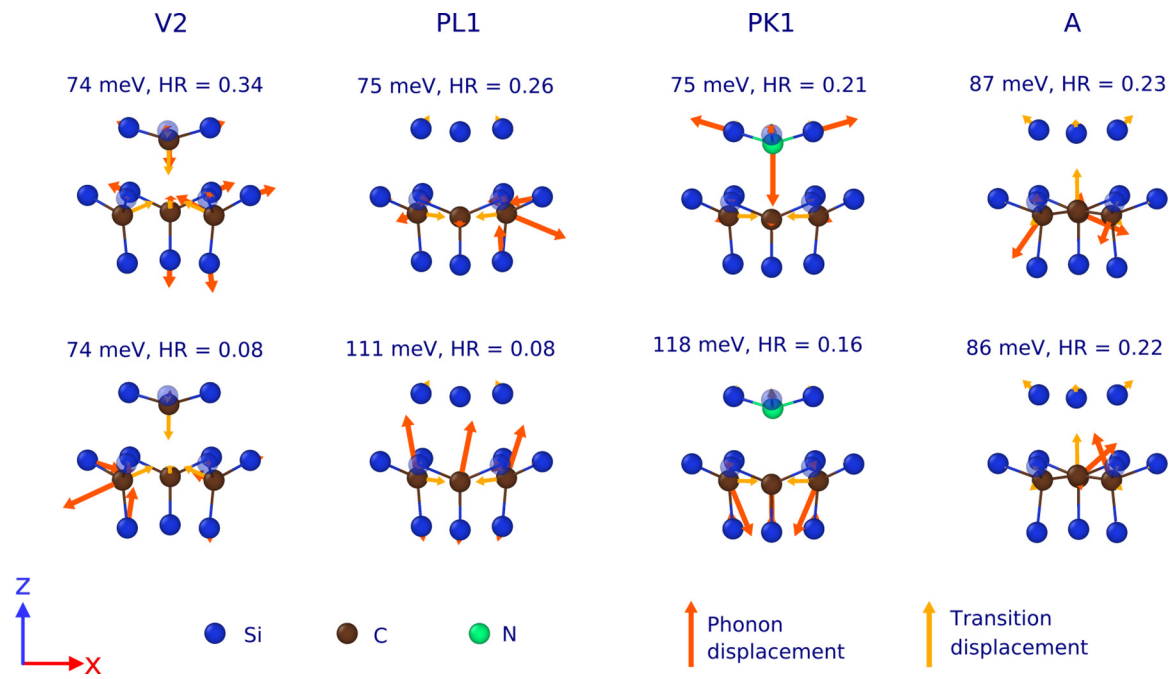

FIG. 6. Transition displacement (the difference of the ground- and excited-state atomic coordinates) and phonon displacement (the atomic movements from the equilibrium positions dictated by the mode's eigenvectors) vectors for a set of selected modes. The transition displacement vectors are amplified by a factor of 20, and the phonon displacement vectors are amplified by a factor of 5. Transparent atoms show the atomic positions in a pristine cell. The figure was created using the software OVITO [68].

only slightly. At around 111 meV, we also observe coupling to localized modes with IPRs of around 5. The C atom displacements induced by transitions are almost perpendicular to vibrational motion. The local modes in the A transition are distributed over relatively few atoms. The C_{Si} atom displaces the most during the transition toward the vacant carbon atom upon emission. Carbon atoms around and at the antisite are engaged in the atomic motions. In the PK1 transition at 75 meV, the vibrational mode displaces the nearest Si atoms toward N. The mode at 118 meV, with an IPR of 7, originates from the strong vibrations of C atoms positioned in the same SiC plane as the vacancy. The structure relaxes around the vacant site.

To elucidate the symmetry of the participating phonons, we can decompose the modes that contribute predominantly to the spectral function of PL1 (Fig. 7). To this end, we project the supercell (SC) modes, $\mathbf{v}_\lambda^{\mathrm{SC}}$, onto each of the PUC eigenmodes $\mathbf{v}^{\mathrm{PUC}}$ at the Γ-point,

$$n(\omega) = \sum_\lambda \left|\langle \mathbf{v}^{\mathrm{PUC}} | \mathbf{v}_\lambda^{\mathrm{SC}} \rangle\right|^2 \delta(\omega - \omega_\lambda). \tag{6}$$

This analysis allows us to identify the respective bulk phonons by inspecting the similarity between atomic vibrations contributing to the PSB and unfolded Γ-modes. 4H-SiC has point symmetry group C_{6v}, where A_1, B_1, E_1, and E_2 are the vibrational modes at the Γ-point [71]. Both A_1 and E_1 modes are Raman- and IR-active, E_2 is only Raman-active, while B_1 is optically forbidden. We assign the 23 meV centered peak to the planar optical E_2 modes. The doublets have a splitting of around 1 meV . The peak at 35 meV can originate from a mixed symmetry of planar acoustic (at M) and optical modes with symmetry of E_1 [24]. The combination of axial optical and acoustic modes shapes the spectral function peak at 48 meV . Indeed, we expect similar behavior for other color centers.

IV. CONCLUSIONS

In this work, we have investigated the vibrational and associated optical properties of V_{Si}^{-1}, V_{Si}^{-2}, $V_C V_{Si}$, $V_C C_{Si}$, and $N_C V_{Si}$ defects in 4H-SiC. We compared the vibronic structure of different color centers by evaluating several important

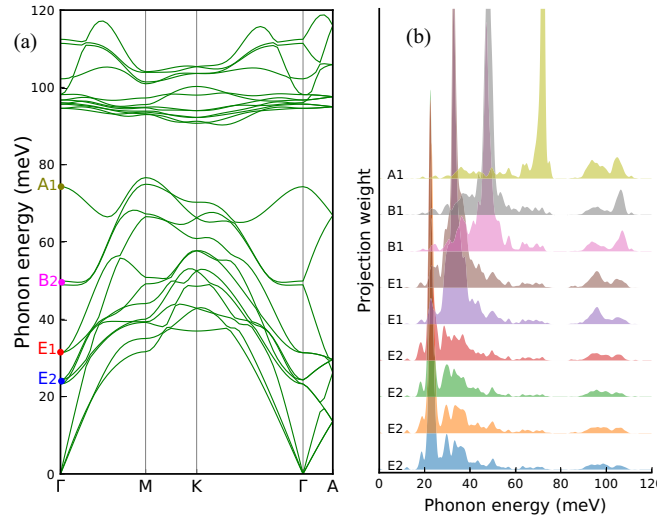

FIG. 7. (a) Phonon dispersion of pristine 4H-SiC along high-symmetry directions. (b) Projection of $(V_C V_{Si})^0_{hh}$ vibrational modes onto modes of the ideal structure (represented by its primitive unit cell). The configuration of the defect is *hh*.

characteristics, such as ZPLs, HRFs, and DWFs, as well as the structure of the PSBs. Our calculated DWFs and PSBs are in excellent agreement with the available experimental data. We found that the effect of the charge state can be great on ZPL and DWF of V_{Si} as it modifies the emission line shape, whereas the line shape does not differ between *hh* and *hk* pairs in $V_C V_{Si}$. The PSB is feature-rich for defects with smaller HRF values, such as single Si vacancies. The electron transfer process to the ground state creates bulk acoustic phonons, and we identified a few narrow peaks that correspond to multiphonon interactions. PSB flattens out for the defect complexes, due to stronger electron-phonon coupling. Furthermore, we predicted a few localized vibrational modes around the phonon band gap that notably contribute to the PL spectra. Overall our work thereby provides a reference database for single-photon sources and spin qubits in 4H-SiC.

ACKNOWLEDGMENTS

This work has been supported by the Academy of Finland under Project No. 311058 and the Knut and Alice Wallenberg Foundation (2014.0226). T.A.-N. has been supported in part by the academy of Finland QTF CoE Grant No. 312298. We also thank CSC-IT Center Science Ltd. (Finland) and the Swedish National Infrastructure for Computing at PDC and NSC (Sweden) for generous grants of computer time. The authors would also like to thank Prof. Martti Puska for his support.

[1] G. R. Fisher and P. Barnes, Philos. Mag. B **61**, 217 (1990).
[2] J. R. Weber, W. F. Koehl, J. B. Varley, A. Janotti, B. B. Buckley, C. G. Van de Walle, and D. D. Awschalom, Proc. Natl. Acad. Sci. USA **107**, 8513 (2010).
[3] P. Mélinon, B. Masenelli, F. Tournus, and A. Perez, Nat. Mater. **6**, 479 (2007).
[4] S. Castelletto and A. Boretti, J. Phys.: Photon. **2**, 022001 (2020).
[5] A. Lohrmann, B. C. Johnson, J. C. McCallum, and S. Castelletto, Rep. Prog. Phys. **80**, 034502 (2017).
[6] I. Aharonovich, D. Englund, and M. Toth, Nat. Photon. **10**, 631 (2016).
[7] D. M. Lukin, C. Dory, M. A. Guidry, K. Y. Yang, S. D. Mishra, R. Trivedi, M. Radulaski, S. Sun, D. Vercruysse, G. H. Ahn, and J. Vuāković, Nat. Photon. **14**, 330 (2020).
[8] D. D. Awschalom, R. Hanson, J. Wrachtrup, and B. B. Zhou, Nat. Photon. **12**, 516 (2018).
[9] N. T. Son, C. P. Anderson, A. Bourassa, K. C. Miao, C. Babin, M. Widmann, M. Niethammer, J. Ul Hassan, N. Morioka, I. G. Ivanov, F. Kaiser, J. Wrachtrup, and D. D. Awschalom, Appl. Phys. Lett. **116**, 190501 (2020).
[10] M. D. Eisaman, J. Fan, A. Migdall, and S. V. Polyakov, Rev. Sci. Instrum. **82**, 071101 (2011).
[11] J. L. O'Brien, A. Furusawa, and J. Vuāković, Nat. Photon. **3**, 689 (2009).
[12] P. Lodahl, S. Mahmoodian, and S. Stobbe, Rev. Mod. Phys. **87**, 347 (2015).
[13] W. B. Gao, A. Imamoglu, H. Bernien, and R. Hanson, Nat. Photon. **9**, 363 (2015).
[14] M. Atatüre, D. Englund, N. Vamivakas, S.-Y. Lee, and J. A. Wrachtrup, Nat. Rev. Mater. **3**, 38 (2018).
[15] B. Hensen, H. Bernien, A. E. Dréau, A. Reiserer, N. Kalb, M. S. Blok, J. Ruitenberg, R. F. L. Vermeulen, R. N. Schouten, C. Abellán, W. Amaya, V. Pruneri, M. W. Mitchell, M. Markham, D. J. Twitchen, D. Elkouss, S. Wehner, T. H. Taminiau, and R. Hanson, Nature (London) **526**, 682 (2015).
[16] S. Bogdanov, M. Y. Shalaginov, A. Boltasseva, and V. M. Shalaev, Opt. Mater. Express **7**, 111 (2017).
[17] A. Boretti, Nat. Photon. **8**, 88 (2014).
[18] C. Lei, S. Peng, C. Ju, M.-H. Yung, and J. Du, Sci. Rep. **7**, 11937 (2017).
[19] D. J. Christle, P. V. Klimov, C. F. de las Casas, K. Szász, V. Ivády, V. Jokubavicius, J. Ul Hassan, M. Syväjärvi, W. F. Koehl, T. Ohshima, N. T. Son, E. Janzén, A. Gali, and D. D. Awschalom, Phys. Rev. X **7**, 021046 (2017).
[20] T. H. Peng, Y. F. Lou, S. F. Jin, W. Y. Wang, W. J. Wang, G. Wang, and X. L. Chen, Powder Diffr. **24**, 311 (2009).
[21] I. J. Wu and G. Y. Guo, Phys. Rev. B **78**, 035447 (2008).
[22] R. Kuate Defo, X. Zhang, D. Bracher, G. Kim, E. Hu, and E. Kaxiras, Phys. Rev. B **98**, 104103 (2018).
[23] L. Gordon, A. Janotti, and C. G. Van de Walle, Phys. Rev. B **92**, 045208 (2015).
[24] Z. Shang, A. Hashemi, Y. Berencén, H.-P. Komsa, P. Erhart, S. Zhou, M. Helm, A. V. Krasheninnikov, and G. V. Astakhov, Phys. Rev. B **101**, 144109 (2020).
[25] P. Udvarhelyi, G. Thiering, N. Morioka, C. Babin, F. Kaiser, D. Lukin, T. Ohshima, J. Ul-Hassan, N. T. Son, J. Vučković, J. Wrachtrup, and A. Gali, Phys. Rev. Appl. **13**, 054017 (2020).
[26] M. Widmann, S.-Y. Lee, T. Rendler, N. T. Son, H. Fedder, S. Paik, L.-P. Yang, N. Zhao, S. Yang, I. Booker, A. Denisenko, M. Jamali, S. A. Momenzadeh, I. Gerhardt, T. Ohshima, A. Gali, E. Janzén, and J. Wrachtrup, Nat. Mater. **14**, 164 (2014).
[27] E. Sörman, N. T. Son, W. M. Chen, O. Kordina, C. Hallin, and E. Janzén, Phys. Rev. B **61**, 2613 (2000).
[28] J. Davidsson, V. Ivády, R. Armiento, N. T. Son, A. Gali, and I. A. Abrikosov, New J. Phys. **20**, 023035 (2018).
[29] W. F. Koehl, B. B. Buckley, F. J. Heremans, G. Calusine, and D. D. Awschalom, Nature (London) **479** (2011).
[30] A. L. Falk, P. V. Klimov, B. B. Buckley, V. Ivády, I. A. Abrikosov, G. Calusine, W. F. Koehl, A. Gali, and D. D. Awschalom, Phys. Rev. Lett. **112**, 187601 (2014).
[31] G. Wolfowicz, C. P. Anderson, A. L. Yeats, S. J. Whiteley, J. Niklas, O. G. Poluektov, F. J. Heremans, and D. D. Awschalom, Nat. Commun. **8**, 1876 (2017).
[32] D. J. Christle, A. L. Falk, P. Andrich, P. V. Klimov, J. U. Hassan, N. T. Son, E. Janzén, T. Ohshima, and D. D. Awschalom, Nat. Mater. **14**, 160 (2015).
[33] T. Umeda, N. T. Son, J. Isoya, E. Janzén, T. Ohshima, N. Morishita, H. Itoh, A. Gali, and M. Bockstedte, Phys. Rev. Lett. **96**, 145501 (2006).
[34] T. Umeda, J. Ishoya, T. Ohshima, N. Morishita, H. Itoh, and A. Gali, Phys. Rev. B **75**, 245202 (2007).
[35] K. Szász, V. Ivády, I. A. Abrikosov, E. Janzén, M. Bockstedte, and A. Gali, Phys. Rev. B **91**, 121201(R) (2015).

[36] S. Castelletto, B. C. Johnson, V. Ivády, N. Stavrias, A. Umeda, T. Gali, and T. Ohshima, Nat. Mater. **13**, 151 (2013).
[37] J. W. Steeds, Phys. Rev. B **80**, 245202 (2009).
[38] A. Csóré, H. J. von Bardeleben, J. L. Cantin, and A. Gali, Phys. Rev. B **96**, 085204 (2017).
[39] S. Hong, M. S. Grinolds, L. M. Pham, D. Le Sage, L. Luan, R. L. Walsworth, and A. Yacoby, MRS Bull. **38**, 155 (2013).
[40] J.-F. Wang, J.-M. Cui, F.-F. Yan, Q. Li, Z.-D. Cheng, Z.-H. Liu, Z.-H. Lin, J.-S. Xu, C.-F. Li, and G.-C. Guo, Phys. Rev. B **101**, 064102 (2020).
[41] H. J. von Bardeleben, J. L. Cantin, E. Rauls, and U. Gerstmann, Phys. Rev. B **92**, 064104 (2015).
[42] S. A. Zargaleh, S. Hameau, B. Eble, F. Margaillan, H. J. von Bardeleben, J. L. Cantin, and W. Gao, Phys. Rev. B **98**, 165203 (2018).
[43] S. A. Zargaleh, H. J. von Bardeleben, J. L. Cantin, U. Gerstmann, S. Hameau, B. Eblé, and W. Gao, Phys. Rev. B **98**, 214113 (2018).
[44] J. Walker, Rep. Prog. Phys. **42**, 1605 (1979).
[45] C. Bradac, W. Gao, J. Forneris, M. E. Trusheim, and I. Aharonovich, Nat. Commun. **10**, 5625 (2019).
[46] J. R. Maze, P. L. Stanwix, J. S. Hodges, S. Hong, J. M. Taylor, P. Cappellaro, L. Jiang, M. V. G. Dutt, E. Togan, A. S. Zibrov, A. Yacoby, R. L. Walsworth, and M. D. Lukin, Nature (London) **455**, 644 (2008).
[47] S. Johnson, P. R. Dolan, T. Grange, A. A. P. Trichet, G. Hornecker, Y. C. Chen, L. Weng, G. M. Hughes, A. A. R. Watt, A. Auffèves, and J. M. Smith, New J. Phys. **17**, 122003 (2015).
[48] X. Yan, P. Li, L. Kang, S.-H. Wei, and B. Huang, J. Appl. Phys. **127**, 085702 (2020).
[49] T. Kobayashi, K. Harada, Y. Kumagai, F. Oba, and Y.-i. Matsushita, J. Appl. Phys. **125**, 125701 (2019).
[50] L. Torpo, T. E. M. Staab, and R. M. Nieminen, Phys. Rev. B **65**, 085202 (2002).
[51] M. Lax, J. Chem. Phys. **20**, 1752 (1952).
[52] T. Miyakawa and D. L. Dexter, Phys. Rev. B **1**, 2961 (1970).
[53] A. Alkauskas, B. B. Buckley, D. D. Awschalom, and C. G. V. de Walle, New J. Phys. **16**, 073026 (2014).
[54] P. E. Blöchl, Phys. Rev. B **50**, 17953 (1994).
[55] G. Kresse and D. Joubert, Phys. Rev. B **59**, 1758 (1999).
[56] G. Kresse and J. Furthmüller, Comput. Mater. Sci. **6**, 15 (1996).
[57] G. Kresse and J. Hafner, Phys. Rev. B **47**, 558 (1993).
[58] J. P. Perdew, A. Ruzsinszky, G. I. Csonka, O. A. Vydrov, G. E. Scuseria, L. A. Constantin, X. Zhou, and K. Burke, Phys. Rev. Lett. **100**, 136406 (2008).
[59] A. V. Krukau, O. A. Vydrov, A. F. Izmaylov, and G. E. Scuseria, J. Chem. Phys. **125**, 224106 (2006).
[60] K. Momma and F. Izumi, J. Appl. Crystallogr. **44**, 1272 (2011).
[61] E. Janzén, A. Gali, P. Carlsson, A. Gällström, B. Magnusson, and N. T. Son, Phys. B **404**, 4354 (2009).
[62] A. Gali, A. Gällström, N. T. Son, and E. Janzén, in *Silicon Carbide and Related Materials 2009*, Materials Science Forum Vol. 645 (Trans Tech, Nürnberg, Germany, 2010), pp. 395–397.
[63] F. Eriksson, E. Fransson, and P. Erhart, Adv. Theory Simul. **2**, 1800184 (2019).
[64] A. Togo and I. Tanaka, Scr. Mater. **108**, 1 (2015).
[65] A. A. Lebedev, Semiconductors **33**, 107 (1999).
[66] A. L. Falk, B. B. Buckley, G. Calusine, W. F. Koehl, V. V. Dobrovitski, A. Politi, C. A. Zorman, P. X.-L. Feng, and D. D. Awschalom, Nat. Commun. **4**, 1819 (2013).
[67] A. L. Crook, C. P. Anderson, K. C. Miao, A. Bourassa, H. Lee, S. L. Bayliss, D. O. Bracher, X. Zhang, H. Abe, T. Ohshima, E. L. Hu, and D. D. Awschalom, Nano Lett. **20**, 3427 (2020).
[68] A. Stukowski, Modell. Simul. Mater. Sci. Eng. **18**, 015012 (2010).
[69] L. Wan, D. Zhao, F. Wang, G. Xu, T. Lin, C.-C. Tin, Z. Feng, and Z. C. Feng, Opt. Mater. Express **8**, 119 (2018).
[70] R. J. Bell, P. Dean, and D. C. Hibbins-Butler, J. Phys. C **3**, 2111 (1970).
[71] D. W. Feldman, J. H. Parker, W. J. Choyke, and L. Patrick, Phys. Rev. **173**, 787 (1968).